

Macroscopic surface tension in a lattice Bhatnagar-Gross-Krook model of two immiscible fluids

I. Halliday,¹ S. P. Thompson,² and C. M. Care²

¹*Division of Applied Physics, School of Science and Mathematics, Sheffield Hallam University, Pond Street, Sheffield, S1 1WB, United Kingdom*

²*Materials Research Institute, Sheffield Hallam University, Pond Street, Sheffield, S1 1WB, United Kingdom*
(Received 28 March 1997; revised manuscript received 10 July 1997)

We present a method by which an interface generating algorithm, similar to that of earlier lattice Boltzmann models of immiscible fluids, may be extended to a two component, two-speed two-dimensional (D2), nine-link (Q9) lattice Bhatnagar-Gross-Krook fluid. For two-dimensional, microcurrent-free planar interfaces between the two immiscible fluids we derive expressions for static interfacial tensions and interfacial distributions of the two fluids. Extending our analysis to curved interfaces, we propose a scheme for incorporating the influence of interfacial microcurrents that is based upon general symmetry arguments and is correct to second order in lattice velocity. The analysis demonstrates that the interfacial microcurrents have only second-order influence upon the macroscopic behavior of the model. We find good agreement between our calculations and simulation results based on the microcurrent stream function and surface tension results from the pressure tensor or Laplace law. [S1063-651X(98)03801-X]

PACS number(s): 47.11.+j, 47.55.Dz, 47.55.Kf, 68.10.-m

I. INTRODUCTION

Formation of emulsions from multicomponent immiscible fluid mixtures is a complex problem of considerable technological and theoretical importance. The utility of traditional numerical methods is inhibited by advection of suspended drops and marked departures in shape before burst. As a result, there is increasing interest in the study of rheological problems by lattice Boltzmann [1–5] and, most recently, dissipative particle dynamics technique [6].

Of the *one-component* lattice Boltzmann schemes available, that which is algorithmically the simplest draws its inspiration from the work of Bhatnagar, Gross, and Krook on the Boltzmann equation of statistical physics. The eponymous *lattice* Bhatnagar-Gross-Krook (BGK) scheme has isotropy and Galilean invariance directly embedded into a technique that benefits from a simple collision step and has been shown to recover single-phase hydrodynamics [4,5]. For these reasons we construct the two-component lattice Boltzmann immiscible lattice-gas (LBILG) model described in Sec. II upon a particular variant of the BGK scheme and not the linearized lattice Boltzmann algorithm of previous work [7]. The variant used is two-dimensional with nine lattice links and is thus designated D2Q9. [5]

Multicomponent immiscible lattice Boltzmann techniques allow one to calculate flows of viscous incompressible fluid mixtures by solving the dynamics of colliding and propagating particles on a regular lattice using a Boltzmann-type equation [1–3] subject to the additional influence of a color-based segregation rule. Recently, the method has been used to simulate deformation and burst in droplets under shear in two dimensions [8,9] and sheared phase separation in three dimensions [10]. The growing literature on the method has been reviewed by Rothmann and Zaleski [11].

It has been argued that small-scale fluid velocity circulations, induced at an interface by the phase segregation rules, are endemic in LBILG simulations [8]. The influence of such microcurrents upon the macroscopic behaviour of LBILG

fluids is therefore of interest. In this paper an analysis similar to that of Gunstensen *et al.* [7,8] is applied to calculate the tension in the interface generated between two D2Q9 BGK fluids.

The model is presented in Sec. II. In Sec. III we present the analysis of the static properties of two prototypical LBILG BGK based interfaces. The results are used to predict surface tension (a) in a plane interface from which symmetry precludes any microcurrent (Sec. IV) and (b) in interfaces where these circulations are present (Sec. V). For clarity, all possible commonality with the work of Gunstensen *et al.* is maintained. In Sec. VI we present details of simulations of our D2Q9 scheme, which are used to obtain mechanical and Laplace law surface tension measurements. The results and conclusions are presented in Sec. VII and VIII, respectively.

II. MODEL

Our model is a BGK scheme similar to that used in [7] but based on a square lattice that supports link density propagation at two speeds and designated D2Q9. Figure 1 and Table I serve to define the nine D2Q9 lattice velocities (links) \mathbf{c}_j and the associated indexing used in this work; we note that \mathbf{c}_9 is a rest direction. The densities that populate the lattice are designated red or blue, $R_i(\mathbf{x}, t)$ [$B_i(\mathbf{x}, t)$] denoting the red [blue] density at position \mathbf{x} , time t moving in direction i . Multi-component fluid behavior arises when segregation is imposed upon such densities by a generalization of the BGK collision to three steps.

First, the usual BGK collision step redistributes achromatic density

$$N_i(\mathbf{x}, t) \equiv R_i(\mathbf{x}, t) + B_i(\mathbf{x}, t) \quad (1)$$

to links using the scalar collision operator ω , which controls fluid shear viscosity through [4,5]

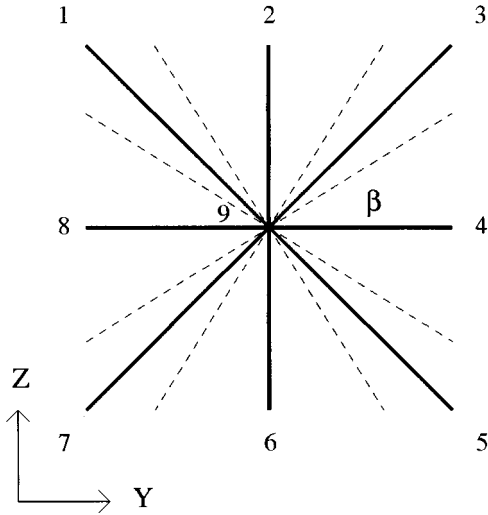


FIG. 1. Lattice link vectors (bold lines) used in the lattice BGK model for the reported simulations. Links indexed by odd values of i subtend an angle of 45° to the horizontal. The angle $\beta = 26.56^\circ$. The angular intervals into which the color field direction must be resolved in order to produce an unambiguous prioritization of link directions are each delimited by one solid and one dashed line.

$$\nu = \frac{1}{6} \left[\frac{2}{\omega} - 1 \right]. \quad (2)$$

In the second collision step the local lattice fluid pressure tensor $P_{\alpha\beta}(\mathbf{x}, t)$, approximated [1,7] by

$$P_{\alpha\beta}(\mathbf{x}, t) = \sum_i N_i(\mathbf{x}, t) c_{i\alpha} c_{i\beta}, \quad (3)$$

is rendered anisotropic at interfacial sites by accumulating (denuding) density on links perpendicular (parallel) to an interface tangent. (The interfacial sites are those that include nonzero densities of both colors.) The motivation for this step is found by reference to the parent lattice-gas techniques (see, e.g., the work of Rothmann and Keller [7]) and is a process not without foundation in hydrodynamics [12]. To achieve this redistribution we follow Gunstensen *et al.* and adjust $N_i(\mathbf{x}, t)$ at mixed nodes by applying a density and momentum conserving perturbation

$$\Delta N_i(\mathbf{x}, t) = \sigma C(\mathbf{x}, t) \cos\{2[\theta_j(\mathbf{x}) - \theta_i]\}, \quad (4)$$

TABLE I. Angular orientations and components of the D2Q9 lattice velocity vectors. NA denotes not applicable.

i	c_{ix}	c_{iy}	c_i^2	θ_i	$\cos(2\theta_i)$
1	-1	1	2	135	0
2	0	1	1	90	-1
3	1	1	2	45	0
4	1	0	1	0	1
5	1	-1	2	-45	0
6	0	-1	1	-90	-1
7	-1	-1	2	-135	0
8	-1	0	1	180	1
9 (rest)	NA	NA	0	NA	NA

where σ is a *surface tension parameter* controlling the amplitude of perturbations, angle θ_i is the angular orientation of link i (Fig. 1), and $\theta_f(\mathbf{x}, t)$ is the direction of a *color field* $\underline{f}(\mathbf{x}, t)$, defined by

$$\underline{f}(\mathbf{x}, t) = \sum_{i,j} [R_j(\mathbf{x} + \mathbf{c}_i, t) - B_j(\mathbf{x} + \mathbf{c}_i, t)] \mathbf{c}_i, \quad (5)$$

where the underline denotes a vector quantity. We have also introduced into Eq. (4) a *concentration factor* $C(\mathbf{x}, t)$,

$$C(\mathbf{x}, t) = 1 - \frac{|\rho_R(\mathbf{x}, t) - \rho_B(\mathbf{x}, t)|}{|\rho_R(\mathbf{x}, t) + \rho_B(\mathbf{x}, t)|}, \quad (6)$$

where $\rho_R(\mathbf{x}, t)$ [$\rho_B(\mathbf{x}, t)$] denote the total of the red [blue] densities at the node with position \mathbf{x} . The incorporation of the concentration factor (6) into the perturbation makes evolution outside the interfacial region exactly the same as in the monophasic model and removes the possibility of surface tension being activated by *one-color* density gradients, as is the case in the ‘‘classical’’ immiscible lattice gas (ILG), where the presence of an interface induces changes that may be ‘‘felt,’’ in the case of interactions between droplets, at distances of several lattice units. Thus the range of interactions is likely to be reduced by the use of the rules encapsulated in Eqs. (4)–(6), which may prove advantageous for certain applications.

In the third and final step, nodal color $\rho_B(\mathbf{x}, t)$, $\rho_R(\mathbf{x}, t)$ is allocated to link densities in that distribution which maximizes the work done by *color flux* $q(\mathbf{x}, t) \equiv \sum_i [R_i(\mathbf{x}, t) - B_i(\mathbf{x}, t)] \mathbf{c}_i$ against the direction of $\underline{f}(\mathbf{x}, t)$ [7]. Clearly, to achieve maximum segregation as much red (blue) as possible should color the density on the link \mathbf{c}_j of largest (smallest) projection onto the direction of $\underline{f}(\mathbf{x}, t)$. As the multi-speed nature of our lattice affects any prioritization of links for color allocation, an unambiguous hierarchy for red population of links 1–9 requires that $\underline{f}(\mathbf{x}, t)$ be resolved into the 16 angular intervals identified in Fig. 1. Then, for example, the prioritization of links 1–9 that results when $\underline{f}(\mathbf{x}, t)$ is found to lie in angular interval β is, in descending order, $i = 3, 4, 5, 2, 9, 6, 1, 8, 7$. The need to resolve $\underline{f}(\mathbf{x}, t)$ into 16 intervals emerges as one attempts to determine which of links $i = 2$ or 5 is *third* most favorable for red occupation, for such prioritization can be made only after determining the direction onto which short link 2 and long link 5 have equal projection. The latter is specified by the angle $\beta = 26.56^\circ$. Symmetry then requires that the positive quadrant is resolved into the four angular intervals shown (Fig. 1). Note that link $i = 9$ (rest) will always have priority 5. The propagate step in which all densities are translated by the appropriate velocity vector is carried out in the usual way on each red and blue density.

In an immiscible lattice-gas cellular automaton [7], the color field cannot influence the outcome of *monochromatic* collisions. Thus sites of high average color purity are relatively unaffected by the presence of a color field. It is this fact and the need to promote a tractable model that motivate our inclusion into the perturbation of the additional factor $C(\mathbf{x}, t)$.

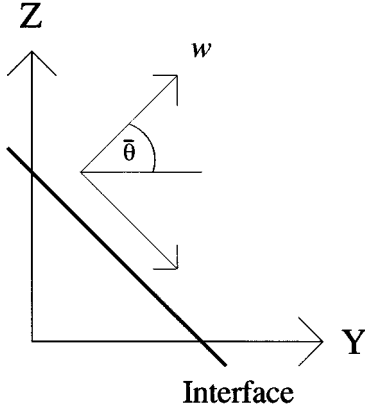


FIG. 2. Coordinate system used in the region of a planar interface.

III. ANALYSIS OF THE MODEL

Throughout we assume there to be sufficient local flatness for the mechanical definition of surface tension [12]:

$$\Sigma = \int_{-\infty}^{\infty} [P_N(w) - P_T(w)] dw \quad (7)$$

to be applicable, where w measures distance normal to the plane of the interface (Fig. 2), i.e., we assume that $P_N(w) \rightarrow P_T(w)$ quickly, as w increases. We postulate that the principal modification necessary to account for interfacial curvature derives solely from the phenomenological inclusion of the microcurrent. We consider the structure of the *steady-state* interface and therefore omit the time t from all quantities throughout the following analysis.

Consider a stable planar interface, separated about a well-defined line, a situation, if that line is appropriately selected (parallel with a lattice link direction \mathbf{c}_i), has sufficient transitional symmetry (parallel to the interface) to preclude variation between adjacent interfacial sites' color gradient $f(\mathbf{x}, t)$. The latter [coinciding with the interfacial normal and thereby the direction of the contour of integration in Eq. (7)] may therefore be characterized by the constant angle $\bar{\theta}$ subtended at the horizontal y axis (Fig. 2). These assumptions are justified by such a situation being readily realizable in appropriately initialized lattice Boltzmann (LB) simulations [7], but note that interfacial *fluctuations* (indigenous in any class of direct simulation employing discrete particles) are present in the parent ILG technique [13,14]. However, even in the context of the ILG, a calculation, founded on assumptions similar to ours and performed within the Boltzmann approximation [1], may be employed to calculate surface tension from a prediction of the structure of the ensemble-average interface at steady state [14]. Adler, d'Humieres, and Rothman also demonstrate [14] that ILG interface fluctuations broadly obey classical statistics, but, importantly for the present work, similar fluctuations in the interfacial behavior of lattice BGK (LBGK) interfaces are not observed for the cases we consider here. We return to this point in Sec. IV. Although some similar effect might be inserted deliberately, the absence of such fluctuations from LBGK calculations is what originally motivated the model [7].

Pressure tensor contractions, analogous to those in Eq. (7), are obtained using Eq. (3) as usual:

$$P_N(\mathbf{x}) = \sum_i N_i c_{iN}^2, \quad (8)$$

$$P_T(\mathbf{x}) = \sum_i N_i c_{iT}^2, \quad (9)$$

where c_{iT} (c_{iN}) denotes that component of \mathbf{c}_i tangential (normal) to the interface:

$$c_{iN}(\mathbf{x}) = |\mathbf{c}_i| \cos(\theta_i - \bar{\theta}), \quad c_{iT}(\mathbf{x}) = |\mathbf{c}_i| \sin(\theta_i - \bar{\theta}). \quad (10)$$

Following Ref. [7], Eq. (7) is considered as an average over M_0 adjacent, long integration lines $z = \text{const}$ and then cast as a discrete summation over lattice nodes in the *area* A so defined (Fig. 2):

$$\begin{aligned} \Sigma &= \int_{w=-\infty}^{\infty} [P_N(w) - P_T(w)] dw \\ &\rightarrow \frac{\cos(\bar{\theta})}{M_0} \sum_{\mathbf{x} \in A} \sum_i N_i(\mathbf{x}) U_i, \end{aligned} \quad (11)$$

in which the summation on \mathbf{x} is over all $\mathbf{x} \in A$ and we have introduced, following Eq. (10) and the notation of Ref. [7],

$$U_i(\mathbf{x}) \equiv (c_{iN}^2 - c_{iT}^2) = c_i^2 \cos[2(\theta_i - \bar{\theta})]. \quad (12)$$

Note that while it is independent of $\bar{\theta}$ (Sec. V), the factor $\cos(\bar{\theta})/M_0$ in Eq. (11) is retained for the sake of compatibility with the work of Ref. [7]. $N_i(\mathbf{x})$ devolves, for D2Q9, into *equilibrium* and *nonequilibrium* parts [4,5]:

$$N_i^{\text{noneq}}(\mathbf{x}) \equiv N_i(\mathbf{x}) - N_i^{\text{eq}}(\mathbf{u}), \quad (13)$$

$$N_i^{\text{eq}}(\mathbf{u}) = t_i (1 + 3u_\alpha c_{i\alpha} - \frac{3}{2}u_\alpha u_\alpha + \frac{9}{2}u_\alpha u_\beta c_{i\alpha} c_{i\beta}), \quad (14)$$

$$t_i = \begin{cases} \frac{1}{36}\rho, & i = 1, 3, 5, 7 \\ \frac{1}{9}\rho, & i = 2, 4, 6, 8 \\ \frac{4}{9}\rho, & i = 9. \end{cases} \quad (15)$$

We note that the \mathbf{x} dependence of $N_i^{\text{eq}}(\mathbf{u})$ arises only through the \mathbf{x} dependence of the velocity field; however, N_i^{noneq} will depend upon \mathbf{x} through both the velocity and its gradients. Using Eqs. (12) and (13), Eq. (11) may be rewritten as

$$\begin{aligned} \Sigma &= \frac{\cos(\bar{\theta})}{M_0} \sum_{\mathbf{x}} \sum_i N_i^{\text{eq}}(\mathbf{u}) U_i(\mathbf{x}) \\ &\quad + \frac{\cos(\bar{\theta})}{M_0} \sum_{\mathbf{x}} \sum_i N_i^{\text{noneq}}(\mathbf{x}) U_i(\mathbf{x}), \end{aligned} \quad (16)$$

the two contributions to which we proceed to treat separately. Using Eqs. (14) and (15), we find by evaluation with a standard computer algebra package, and confirmed by direct evaluation, that

$$\sum_{\mathbf{x}} \sum_i N_i^{\text{eq}}(\mathbf{u}) U_i(\mathbf{x}) = \sum_{\mathbf{x}} \rho u^2 \cos\{2[\theta_u(\mathbf{x}) - \bar{\theta}]\}, \quad (17)$$

where we have introduced $\theta_u(\mathbf{x})$ such that

$$u_x = u \cos[\theta_u(\mathbf{x})], \quad u_y = u \sin[\theta_u(\mathbf{x})]$$

and we have used the components of \mathbf{c}_i defined in Table I. To deal with the *second* term on the right-hand side of Eq. (16) we follow Gunstensen *et al.* and appeal to the lattice Boltzmann equation for the BGK algorithm, appropriately modified to account for the presence of interfacial achronatic density perturbations and adapted to the steady state [7]:

$$N_i(\mathbf{x} + \mathbf{c}_i) = N_i(\mathbf{x}) - \omega N_i^{\text{noneq}}(\mathbf{x}) + \Delta N_i(\mathbf{x}). \quad (18)$$

Noting, for a closed lattice, that $\sum_{\mathbf{x}} N_i(\mathbf{x} + \mathbf{c}_i) = \sum_{\mathbf{x}} N_i(\mathbf{x})$ and using Eq. (4), one obtains after some algebra

$$\begin{aligned} \sum_{\mathbf{x}} \sum_i N_i^{\text{noneq}}(\mathbf{x}) U_i &= \frac{\sigma}{\omega} \sum_{\mathbf{x}} C(\mathbf{x}) \sum_i \cos[2(\theta_i - \bar{\theta})] U_i \\ &= \frac{\sigma}{\omega} [6 - 2 \cos(4\bar{\theta})] \sum_{\mathbf{x}} C(\mathbf{x}), \end{aligned} \quad (19)$$

which we note has the expected fourfold rotational symmetry. Incorporating Eqs. (17) and (19) into Eq. (16) yields an expression for macroscopic surface tension:

$$\begin{aligned} \Sigma(\sigma, \omega) &= \frac{\cos(\bar{\theta})}{M_0} \sum_{\mathbf{x}} \rho \mathbf{u}^2 \cos\{2[\theta_u(\mathbf{x}) - \bar{\theta}]\} \\ &\quad + \frac{\sigma \cos(\bar{\theta})}{M_0 \omega} [6 - 2 \cos(4\bar{\theta})] \sum_{\mathbf{x}} C(\mathbf{x}). \end{aligned} \quad (20)$$

Reminding the reader that $\cos(\bar{\theta})/M_0$ is independent of $\bar{\theta}$, we remark that Eq. (20) for $\Sigma(\sigma, \omega)$ is correct to all orders of fluid velocity. The second term on its right-hand side is relatively straightforward to evaluate if we remember that $C(\mathbf{x})$ vanishes at pure, noninterfacial sites. No simplification is evident in the first term of Eq. (20), however, and the positional summation must be evaluated over all $\mathbf{x} \in A$. Notwithstanding, to leading order in \mathbf{u} its contribution to $\Sigma(\sigma, \omega)$ at practical values of σ (see Sec. VII) is small. In this regime, therefore, $\Sigma(\sigma, \omega) \sim \sigma/\omega$, where we recall that ω determines lattice fluid kinematic viscosity through Eq. (2). To the same order of approximation, Gunstensen *et al.* reported an analogous dependence of their Σ upon their LBILG collision parameter λ^{-1} , where λ is the eigenvalue of the LBILG collision matrix that determines the simulated fluid kinematic viscosity.

IV. SURFACE TENSION IN PLANE INTERFACES

A. Plane interface parallel to the z axis

Throughout this and subsequent sections we take a microcurrent to be an interfacial effect resulting in a nonzero mass flux across a line parallel to a static interface and we do not consider further microcurrents defined in alternative terms, which produce no mass flux on mesoscopic length

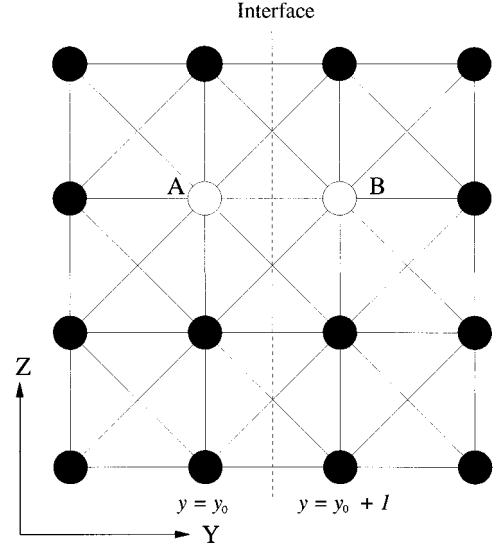


FIG. 3. Symmetry of populations in a vertical interface. This figure shows a lattice excerpt containing several mixed nodes of which two have been highlighted (open circles) in an interface centered on the dashed line. Nodes to the left are predominantly red ($\rho_R \gg \rho_B$) while, in the stable interface, those to the right are predominantly blue ($\rho_B \gg \rho_R$). Note that color populations in nodes A and B are equivalent under color reversal and rotation through 180° . The dotted line indicates the initial interface.

scales and have no physical influence on surface tension. Consider a steady-state planar interface parallel to short lattice links along the z axis in which color is symmetrically separated (Fig. 3), so $\cos(\bar{\theta})=1$. Translational symmetry along the z axis implies an absence of any microcurrent and a color gradient $\hat{f}(\mathbf{x}) = f(y)\hat{y}$. It is appropriately illustrative of the notable stability of the LB techniques in general that the direction of the color field in the final steady state is free of any fluctuations. For purposes of verification, the direction of the color field measured from simulation showed no measurable departure from this assumption. Note, however, that even for the plane geometries considered here, cellular automata based ILG simulations would contain *fluctuating* interfaces, even at “steady state.”

For these initial lattices, we consider that the stable interface cannot be centered on a single layer and will require a minimum thickness of two layers, say, $y = y_0$ and $y_0 + 1$, and a color distribution symmetrical under color reversal, corresponding to a concentration given by

$$C(\mathbf{x}) = C(\delta(y - y_0) + \delta(y - y_0 - 1)), \quad (21)$$

where C is a constant. If there are no microcurrents, $\mathbf{u} = \mathbf{0}$ everywhere and the expression for the surface tension reduces to

$$\begin{aligned} \Sigma(\sigma, \omega) &= \frac{4\sigma C}{M_0 \omega} \sum_{z=1, \dots, M_0} \forall y [\delta(y - y_0) + \delta(y - y_0 - 1)] \\ &= \frac{8\sigma C}{\omega}. \end{aligned} \quad (22)$$

At steady state, when the color content of each node must be constant between successive steps, links connecting two mixed sites should contain, at each end, counter-propagating equal densities of each color. If it is further assumed that achromatic link densities depart only negligibly from their rest equilibrium values t_i , the value of the constant C in Eq. (21) may be calculated.

Each interfacial site connects to three other mixed nodes and three monochromatic sites in the y direction and with two equivalent sites in the z direction (Fig. 3). We assume in the following that the sites are pure red for $y < y_0$ and pure blue for $y > y_0 + 1$. For diagonal, “speed 2,” links $i=3,5$ in $y=y_0$ interacting with links $i=7,1$ in $y=y_0+1$:

$$R_3(y_0, z) = B_3(y_0, z) = R_5(y_0, z) = B_5(y_0, z) = \frac{1}{2}t_1 = \frac{1}{72}\rho_0,$$

$$\begin{aligned} R_1(y_0+1, z) &= B_1(y_0+1, z) = R_7(y_0+1, z) = B_7(y_0+1, z) \\ &= \frac{1}{2}t_1 = \frac{1}{72}\rho_0, \end{aligned}$$

and similarly for the speed 1 link $i=4$ in $y=y_0$ interacting with link $i=8$ in $y=y_0+1$:

$$R_4(y_0, z) = B_4(y_0, z) = \frac{1}{2}t_2 = \frac{1}{18}\rho_0,$$

$$R_8(y_0+1, z) = B_8(y_0+1, z) = \frac{1}{18}\rho_0,$$

where ρ_0 is the achromatic density of the interfacial lattice node and we have used identities (15). With this information the color density of the nodes in $y=y_0$ may be calculated:

$$\begin{aligned} \rho_B(y_0, z) &= B_3(y_0, z) + B_4(y_0, z) + B_5(y_0, z) \\ &= \left(\frac{1}{72} + \frac{1}{72} + \frac{1}{18}\right)\rho_0 = \frac{1}{12}\rho_0, \end{aligned}$$

$$\rho_R(y_0, z) = \rho_0 - \frac{1}{12}\rho_0 = \frac{11}{12}\rho_0,$$

whence, from Eq. (6), $C = \frac{1}{6}$. This value for C , on insertion into Eq. (22), gives, for our model of a horizontal interface parallel to the short D2Q9 lattice links, a macroscopic surface tension

$$\Sigma(\sigma, \omega) = \frac{4\sigma}{3\omega}. \quad (23)$$

B. Plane diagonal interface

For a steady *diagonal* plane interface separated in a line parallel to the longer lattice links (Fig. 4) two different (but simply related) cross-interface density profiles occur. However, the macroscopic surface tension can be calculated with a small modification. In the simplest case of an interface constituted by mixed sites A, B in adjacent sections aa', bb' (Fig. 4) densities at A , $\{R_i(A), B_i(A)\}$, and those at B , $\{R_i(B), B_i(B)\}$, are equivalent under combined color reversal and a two-fold rotation. If the achromatic densities are again assumed to depart negligibly from their rest equilibrium values t_i , the simplest distribution of color through this diagonal interface may be deduced. For links in the only (mainly red) mixed node in section aa' (Fig. 4), connecting to the mixed mainly blue node in two bb' sections, postcollision densities are

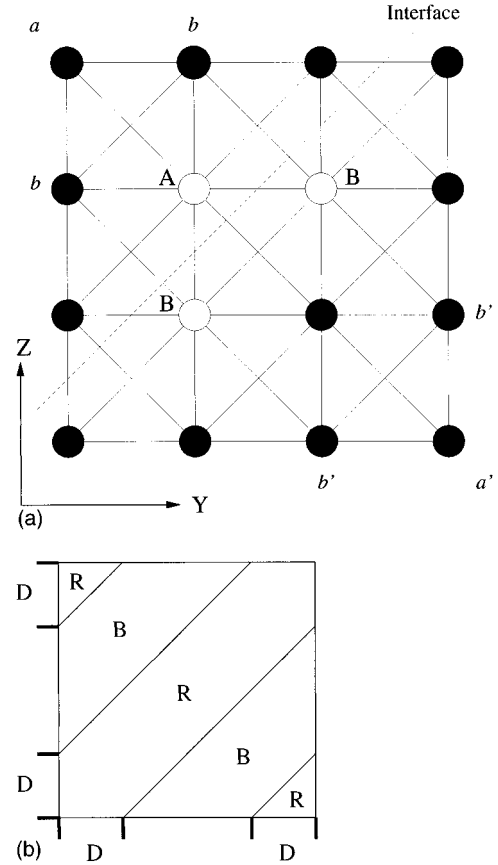


FIG. 4. (a) Populations in a diagonal interface. This figure shows a lattice excerpt containing several mixed nodes of which three have been highlighted (open circles) in the interface centered on the dashed line. Nodes above the dashed line are predominantly red ($\rho_R \gg \rho_B$), while, in the stable interface, those below are predominantly blue ($\rho_B \gg \rho_R$). Populations in nodes A and B are again equivalent under color reversal and rotation through 180° . (b) Initial distribution of color for the simulation of a diagonal interface on the square D2Q9 lattice showing the periodic images of the red diagonal layer in the box corners. Regions marked R (B) correspond to red (blue) mass. Distance $D=27$ lattice units.

$$R_4(A) = B_4(A) = R_6(A) = B_6(A) = \frac{1}{2}t_2 = \frac{1}{18}\rho_0, \quad (24)$$

while for link 5 in section aa' connecting to a pure blue node

$$R_5(A) = 0, \quad B_5(A) = t_1 = \frac{1}{36}\rho_0, \quad (25)$$

where we have again used identities (15). Densities for the mixed B node are easily obtained from the symmetry arguments already rehearsed. The color density of the mixed nodes in the diagonal interface is therefore

$$\rho_B(A) = B_5(A) + B_4(A) + B_6(A) = \left(\frac{1}{36} + \frac{1}{18} + \frac{1}{18}\right)\rho_0 = \frac{5}{36}\rho_0, \quad (26)$$

$$\rho_R(A) = \rho_0 - \frac{5}{36}\rho_0 = \frac{31}{36}\rho_0, \quad (27)$$

whence, from Eq. (6), $C = \frac{5}{18}$ for both the A and B mixed sites. Setting $\theta = 45^\circ$ and noting that there is an A and a B

mixed site on any horizontal line crossing a diagonal interface, it follows from Eq. (20) that the macroscopic surface tension is

$$\Sigma(\sigma, \omega) = \frac{40\sigma}{9\sqrt{2}\omega}. \quad (28)$$

The preceding analysis of flat interfaces between static fluids neglects perturbation-induced departures from equilibrium rest density, the validity of which assumption increases with decreasing perturbation amplitude σ and is supported from the results of Sec. V. It should be noted that this assumption implicitly restricts the principal analytical results of this section [Eqs. (23) and (28)] to apply when the induced macroscopic surface tension is small. Note also that due to the absence of local curvature in the interface no density (pressure) change between the bulk fluids separated by the interface is to be expected. Moreover, the fact that, for the present model in the case of, e.g., the vertical interface along the z direction, the population of link 4 may, on general grounds, be different from that of links 3 and 5 allows for density to be constant through the interface. We now consider the effect of microcurrents that are precluded by symmetry in planar interfaces.

V. SURFACE TENSION IN CURVED INTERFACES

Microcurrents are normally induced close to an interface by the segregating effect of the surface tension rule [8,9,15]; only in the presence of suitable symmetry, such as the cases considered in Sec. IV, will the microcurrents be absent. The presence of interfacial curvature and a gradient in the color field mean makes it impossible to argue on general grounds that an interfacial microcurrent should be absent from the rest interface. Its influence will be felt principally through the first term in Eq. (20). The magnitude of the microcurrent velocity close to the interface has been observed [8,15] to be of the form

$$u = u(\mathbf{x})\sigma. \quad (29)$$

For circular interfaces in two-dimensional simulations of static (say) red drops, the interfacial microcurrent pattern must conform with the rotational symmetry of the underlying lattice and two complementary, counterrotating microcurrent *cells* must occupy any lattice quadrant, the maximum velocity in each occurring close to the generating interface (Fig. 6). In fact, the maximum value of the surface tension inducing perturbation occurs for the maximum value of U_i in Eq. (12) at $\bar{\theta} = 45^\circ$, accounting for the fact that the microcurrent circulation close to the interface is radial along the diagonal bisectors of each quadrant (Fig. 6). Moreover, on grounds of lattice symmetry and hydrodynamics (which must ultimately govern the microcurrent), one expects the extent of a microcurrent cell to be determined by lattice extremities and drop radius R . We approximate the flow in a microcurrent cell outside the interface with a uniform rotation such that its outermost streamline touches the interface and has a velocity determined principally by σ . We then write the microcurrent velocity field $u(\mathbf{x}) = u(\hat{r}, |r|/R)$ in Eq. (25) and note that

$u(\hat{r}, |r|/R)$ must have the fourfold rotational symmetry of the lattice. Hence Eq. (20) becomes

$$\begin{aligned} \Sigma = & \frac{\sigma^2 \cos(\bar{\theta})}{M_0} \sum_{\mathbf{x}} u(\hat{r}, |r|/R)^2 \rho \cos\{2[\theta_u(\mathbf{x}) - \bar{\theta}]\} \\ & + \frac{\sigma \cos(\bar{\theta})}{M_0 \omega} [6 - 2 \cos(4\bar{\theta})] \sum_{\mathbf{x}} C(\mathbf{x}). \end{aligned} \quad (30)$$

This result, it should be noted, applies only to the D2Q9 BGK model through the assumed form of the equilibrium distribution function defined in Eqs. (14) and (15) and introduced by Qian, d’Humières, and Lallemand [5]. Clearly, the potential for anisotropy entailed in the second term therefore applies only to the model under consideration here and the actual extent of any anisotropy in surface tension may be determined only after $C(\mathbf{x})$ is known. To interpret Eq. (30) in the presence of curvature, we consider an interfacial element of length $R\Delta\theta$ from a large circular drop of radius R , subtending a small angle $\Delta\theta$ at the drop center. This element we assume to be locally flat and contained within an area defined by M_0 long horizontal lattice lines $z = \text{const}$. Then $M_0 = R\Delta\theta \cos(\bar{\theta})$, whence $\cos(\bar{\theta})/M_0 = 1/R\Delta\theta$. The magnitude of the positional summation in the second term of Eq. (30) will be proportional to $R\Delta\theta$ and a form $\sigma k_2/\omega$ is assumed. With respect to the first term, we take the microcurrent activity to decay rapidly away from the interface (an assumption supported by the results of Fig. 7) and this will yield finite contributions to the first summation only from a number of sites proportional in number to the $R\Delta\theta$ and the velocity at all of these sites we take to be determined principally by σ . The positional summation in the first term in Eq. (30) will therefore also be proportional to $R\Delta\theta$ and we assume a form $\sigma^2 k_1$. For the interfacial tension of a drop we therefore find

$$\Sigma(\sigma, \omega) = \sigma^2 k_1 + \frac{\sigma}{\omega} k_2, \quad (31)$$

in which for small values of the perturbation parameter σ , the dominant contribution is from the second term and hence

$$\Sigma(\sigma, \omega) \cong \frac{\sigma}{\omega} k_2. \quad (32)$$

VI. SIMULATION

In order to make a comparison with the calculations for plane interfaces we construct an effectively infinite system and thus periodic boundaries were used all around a square lattice and retained for all other simulations reported here. A suitable box size and equilibration time were determined on the basis of stability. For all the data presented, sites were initialized to achromatic density $\rho_0 = 1.8$ with rest equilibrium link densities of 0.8, 0.18, and 0.045 for speed 0, 1, and 2 links, respectively, the initial color being allocated so as to produce a particular interface configuration.

Results were obtained for plane, $y = \text{const}$, interfaces on a 120×120 lattice containing a red vertical layer sandwiched between two blue fluids. The initial interface lay between consecutive y planes of nodes and the red layer was defined

TABLE II. Calculated and measured values of the Laplace law surface tension. Calculated values are derived from Eqs. (23) and (28). For the planar horizontal interface $(\sigma, \omega) = (5 \times 10^{-3}, 0.91)$, while for the planar diagonal interfaces simulated $(\sigma, \omega) = (5 \times 10^{-4}, 0.91)$.

Interface orientation	Calculated $\Sigma(\sigma, \omega)$	Measured $\Sigma(\sigma, \omega)$	Calculated C	Measured C
horizontal	7.33×10^{-3}	7.37×10^{-3}	0.166	0.15
diagonal	1.73×10^{-3}	1.73×10^{-3}	0.28	0.28

by $\rho_R(x, y) = 1.8$ and 0 , $39 < y < 81$. The diagonal interface was constructed by initializing as red those nodes which lay on the lattice of Fig. 4(b) with y coordinates such that $z - 26 \leq y \leq z + 26$, with the periodic images of this red layer incorporated in the lattice corners [Fig. 4(b)]. An equilibration time of 15 000 updates was allowed for both plane interface orientations and the steady-state density distribution was measured through the interfacial region. Also measured through the interface was quantity $P_N - P_T$, using Eqs. (8) and (9). These measurements, in conjunction with a simple discrete approximation to the mechanical definition (7), allowed the planar interfacial tension to be evaluated.

Links within a circular, central portion of radius R of an otherwise blue 150×150 lattice were initialized red to form a circular drop. Different combinations of surface tension perturbation parameter σ and BGK collision parameter ω were used to generate stable drops with the values of ω now being chosen so as best to recover classical hydrodynamic behavior [16]. Laplace law measurements were used upon these drops to obtain surface tension $\Sigma(\sigma, \omega)$ from the gradient of pressure difference $\Delta p = \Delta \rho / 3$ [4,5] as a function of $1/R$ for $15 < R < 40$. The steady-state value of R was obtained from the drop inertia tensor [8].

In order to observe the influence of microcurrent activity from circular interfaces the stream function

$$\psi(x, y) = \int_{y=0}^{y'=y} u_y(x, y') dy' \quad (33)$$

was calculated from the velocity field along with the corresponding pressure (lattice density) field. The variation with normalized distance from the drop center $\bar{r} \equiv r/R$, of velocity modulus averaged over an annular lattice sample concentric with the drop center, radius \bar{r} , yields a quantitative measure of microcurrent activity and a test of the assumptions made in deriving Eq. (31).

VII. RESULTS

Consistent with the assumptions made in Sec. II, quiescent color mixing in appropriately initialized plane interfaces was confined to layers of two sites. Table II shows the close agreement between calculated and measured interfacial quantities for both cases of planar interface considered. The measured values of surface tension were obtained directly from a trapezium rule approximation to Eq. (7):

$$\Sigma(\sigma, \omega) = \frac{|\mathbf{c}_i|}{2} \left(\sum_I [P_N(\mathbf{l}) - P_T(\mathbf{l}) + P_N(\mathbf{l} + \mathbf{c}_i) - P_T(\mathbf{l} + \mathbf{c}_i)] \right), \quad (34)$$

where \mathbf{l} denotes position on a lattice line perpendicular to the interface and we use Eqs. (8) and (9) to obtain $P_N(\mathbf{l}), P_T(\mathbf{l})$.

Figure 5(a) shows, on the same axes, normalized variation of color and pressure tensor contraction $[P_N(\mathbf{l}) - P_T(\mathbf{l})]$ through the vertical interface described in Sec. III. For the corresponding case of a diagonal interface [Figs. 5(b) and 5(c)] color is not, as expected, symmetrically distributed about the maximum value of $P_N(\mathbf{l}) - P_T(\mathbf{l})$; Figs. 5(b) and 5(c) represent sections of the interface along adjacent diagonals (Fig. 4) that are interrelated by a rotation of π radians and a color reversal. For the results of Fig. 5 the BGK collision parameter $\omega = 0.91$ was used in conjunction with surface tension perturbations $\sigma = 0.005$ [Fig. 5(a)] and $\sigma = 0.0005$ [Figs. 5(b) and 5(c)].

Figure 6 shows the microcurrent structure generated at the surface of a red drop through the stream function $\psi(x, y)$ calculated by a process of numerical integration after Eq. (33). The microcurrents are seen to be consistent with the symmetry of the underlying lattice and the maximum perturbation. The range of influence of the microcurrent for a periodically bounded drop on a 150×150 lattice is shown in Fig. 7, which charts the variation of $|\mathbf{u}|$, flow speed, against normalized distance from the drop center $|\mathbf{r}|/R$ for several values of parameter σ . As a quantitative assessment we note that Eq. (31) predicts that a graph of $\Sigma(\sigma, \omega)/\sigma$ against $1/\omega$ will have an ordinal intercept (gradient) from which constant k_1 (k_2) may be inferred. Accordingly (Fig. 8), $\Sigma(\sigma, \omega)/\sigma$ was obtained from Laplace's law (see Sec. VI) applied to drops with $0.5 \leq \omega \leq 2.0$ and $\sigma = 0.025$. With the latter value of perturbation parameter the number of data points necessary to apply linear regression reliably entails significant processing, but yields values of 30.55 and 1.26 for k_1 and k_2 . Hence, for $\sigma = 0.025$, the microcurrent contribution to the macroscopic surface tension in our model is seen to approximate to that arising from the second term in Eq. (31) and we infer an estimated upper limit $\sigma \leq 0.025$ such that, for the particular model of the present study, the influence of a microcurrent upon the macroscopic surface tension is of decreasing importance.

Figure 9 concentrates upon values of $0.001 \leq \sigma \leq 0.0125$, well below this upper limit, and shows results for surface tension $\Sigma(\sigma, \omega)$ for $1.5 \leq \omega \leq 1.9$ plotted against the quotient σ/ω ; these results for the surface tension are derived from Laplace law measurements described above. The continuous line represents a linear regression fit to this data and although *unconstrained* to pass through the origin, the fit generates an intercept that lies well within one standard deviation of zero and a gradient that identifies k_2 [Eq. (32)]. Obtained from Eq. (20), Eq. (23) is valid for a flat horizontal interface at rest. Based as it is on the mechanical definition of surface tension [12] [Eq. (20)], we interpret only with respect to equilibrium (rest) fluids and the velocity dependence entailed in its first term, we suggest, should be regarded as arising only from that flow present in a rest simulation: the mi-

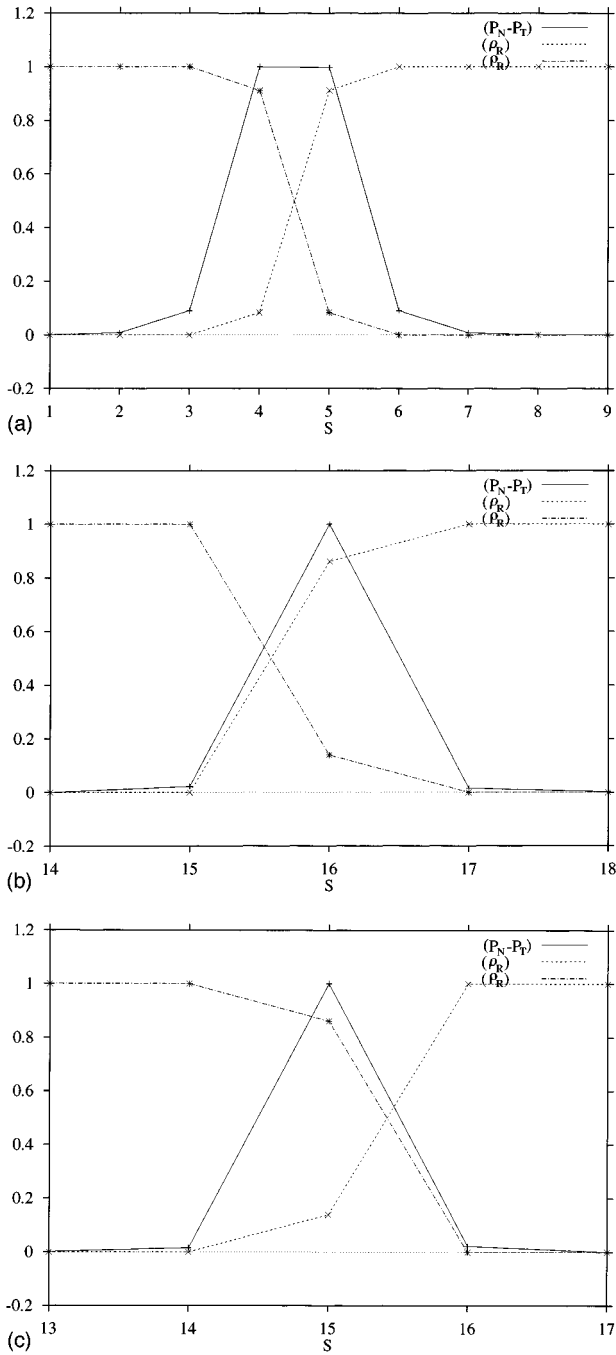
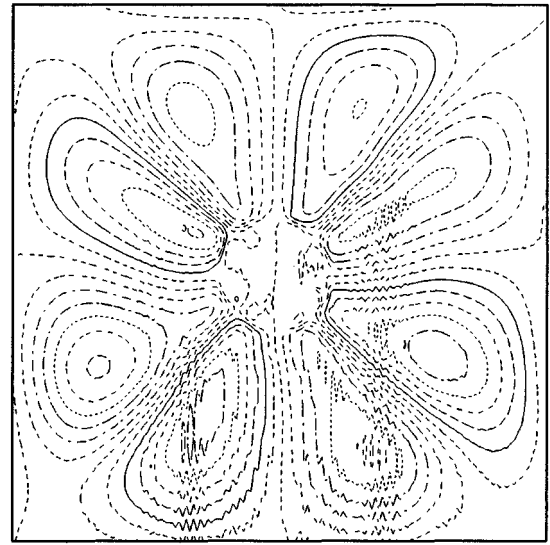
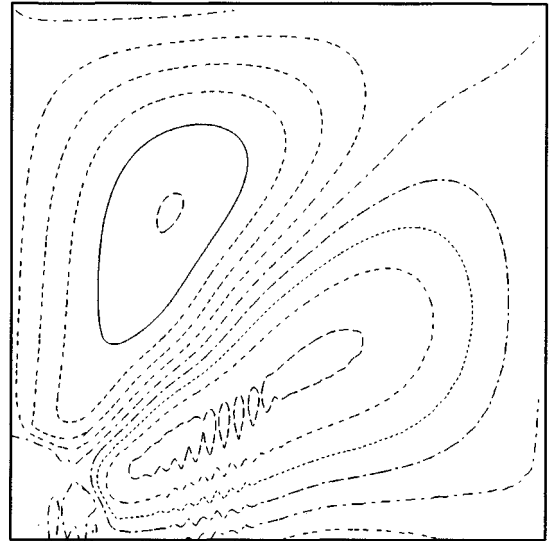


FIG. 5. (a) Normalized variations across a vertical interface, with S measured in lattice units. The dotted (dashed) line connects calculated blue (red) densities and symbols mark corresponding measured values. The solid line corresponds to the value of $P_N - P_T$. The achromatic density in use was $\rho_0 = 1.8$, $\omega = 0.91$, and $\sigma = 0.005$. (b) Normalized variations across a diagonal interface, sampled along aa' (Fig. 4). The parameter s is related to the coordinate y through $s = \sqrt{2}y$. After (a) lines connect calculated points and symbols show results obtained from simulation. The solid line corresponds to the value of $P_N - P_T$. The achromatic density in use was $\rho_0 = 1.8$, $\omega = 0.91$, and $\sigma = 0.005$. As expected, this plot does not show the same color-reversal symmetry as in case of (a); instead the color distribution is related to that displayed in (c); See Sec. IV B. (c) Normalized variations across a diagonal interface, sampled along bb' (Fig. 4). Other parameters are the same as in (b).



(a)



(b)

FIG. 6. Stream function for steady circulation pattern developed by a drop of radius 40 lattice units placed centrally on a square lattice. The flow pattern is observed to be stable after approximately 4000 time steps. The results were obtained for the same simulation parameters as Fig. 5(a).

crocurrent. Nevertheless, a useful check on Eq. (20) may be performed by applying a uniform shear of increasing rate parallel to the flat vertical layer $-10 \leq y \leq 10$ on a 60×60 lattice (see the discussion above and Fig. 3), the shears being generated in the usual manner [8,9]. Setting $\bar{\theta} = 0$ and $\theta_u(\mathbf{x}) = \pi/2$ for small σ , we may omit the second term from Eq. (20) and

$$\Sigma(\sigma, \omega) \sim -\frac{\rho}{M_0} \sum_{\mathbf{x}} \mathbf{u}^2 = -\rho \sum_{y=-10}^{y=20} \mathbf{u}(y)^2. \quad (35)$$

Figure 10 shows the results of plotting $\Sigma(\sigma, \omega)$, obtained from Eq. (34), as the ordinate against summation $S_0 \equiv \sum_{y=-10}^{y=20} \mathbf{u}(y)^2$, obtained for a small range of shear rates, as the abscissa, with the expected linear trend emerging. At

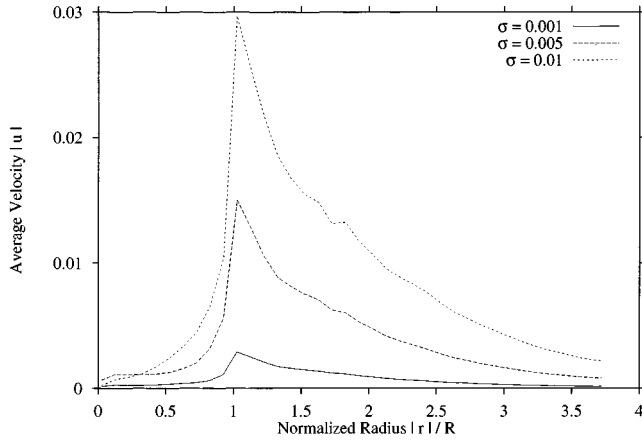


FIG. 7. Variation of $|\mathbf{u}|$, microcurrent flow speed measured in units of lattice spacing per time step, against normalized distance from the drop center $|r|/R$ for several values of parameter σ (see key). Note the approximately linear trend in peak flow activity with σ , which occurs close to the interface.

smaller shear rates the (constant, positive) contribution of the first term in Eq. (20) begins to become apparent. It is important to note that, for the reasons set out above, we do not claim that Fig. 10 represents more than an interesting property of Eq. (20), Eqs. (20) and (30) resting on definitions in which a static interface is implicit [12].

VIII. CONCLUSIONS

We have presented a method by which the interface generating algorithm of Gunstensen *et al.*, itself an extension of the automaton-based algorithm of Rothman and Keller [7], may be successfully extended to a D2Q9 lattice BGK scheme and generalized to promote both tractability and correspondence with the progenitor cellular automaton technique. As Table II shows, simulation measurements of sur-

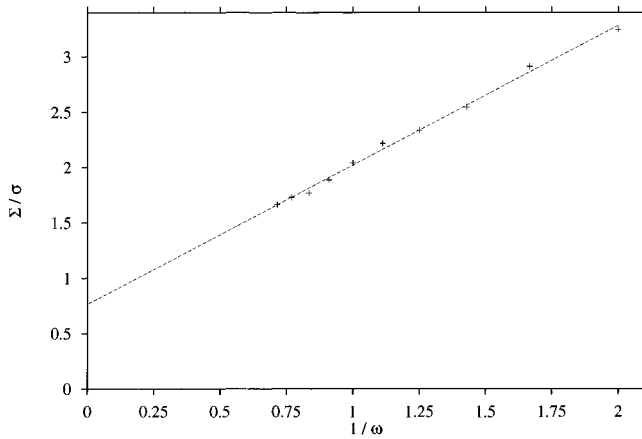


FIG. 8. Simulational measurements of the Laplace law surface tension $\Sigma(\sigma, \omega)$ (measured in lattice units) for $0.001 \leq \sigma \leq 0.0125$, $1.5 \leq \omega \leq 1.9$ as a function of quotient σ/ω (where σ and ω are dimensionless). The continuous line is a linear regression fit to the data.

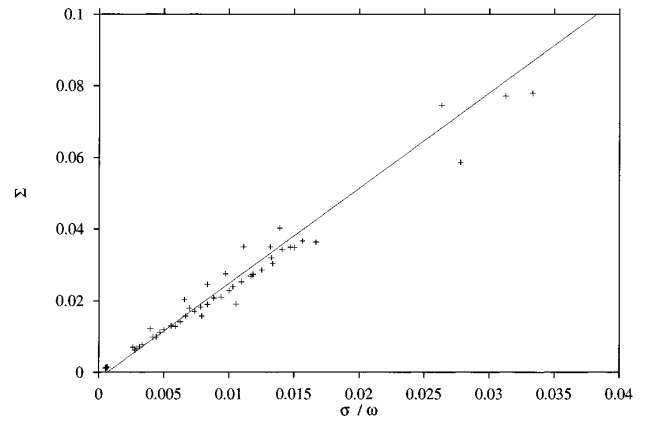


FIG. 9. Plot of $\Sigma(\sigma, \omega)/\sigma$ (measured in lattice units) against (dimensionless) $1/\omega$ for $0.5 \leq \omega \leq 2.0$. The former were obtained from Laplace's law applied to drops with $\sigma=0.025$ and $15 \leq R \leq 40$ on a 150×150 lattice.

face tension and cross-interfacial color distributions for this model are in good agreement with those values calculated from analysis of our algorithm, for both plane horizontal and diagonal microcurrent-free interfacial orientations. The difference between the two expressions suggests an orientational-dependent anisotropy in the model's surface tension and the effect of this upon shape in drops simulated by this method is currently under study. We have deduced, on general grounds, the structure of the microcurrent circulation generated by circular drops and compared these with measurements. These measurements demonstrate that the simple theory successfully accounts for the broad structure of the microcurrent flow field. The analysis allows us to develop an expression [Eq. (31)] for the surface tension of a drop and this expression demonstrates that the microcurrent velocity field might be expected directly to influence the model's surface tension. For small values of parameter σ the corrections are only found to be second order in σ and this is

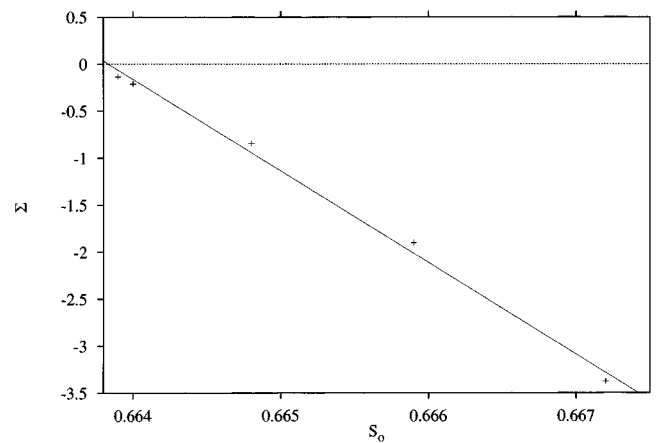


FIG. 10. $\Sigma(\sigma, \omega)$ [measured in lattice units obtained from Eq. (34)] as ordinate against summation $S_0 \equiv \sum_{y=-10}^{y=20} \mathbf{u}(y)^2$ (dimensions of lattice units squared) for a vertical interface exposed to a uniform shears parallel to the vertical interface $-10 \leq y \leq 10$ placed on a 90×60 lattice.

substantiated by the measurements summarized in Fig. 9. Any attempt quantitatively to assess the approximate theory of microcurrent contribution presented here will require substantial quantities of data and should be undertaken only after a more rigorous analysis of the contribution of the first term in Eq. (31). The undertaking would be facilitated by a calculation of the steady microcurrent flow field as an ap-

proximate or numerical solution of the equations of creeping flow, which should fully account for the microcurrent structure. Although our general arguments yield a qualitative insight into the origin of the microcurrent, such a calculation would provide the most useful check on our understanding of this phenomenon and hence upon the ability of the method in the area of its most important potential application.

-
- [1] U. Frisch, D. d'Humieres, B. Hasslacher, P. Lallemand, Y. Pomeau, and J. P. Rivet, *Complex Syst.* **1**, 649 (1987), and references therein.
- [2] G. McNamara and G. Zanetti, *Phys. Rev. Lett.* **61**, 2332 (1988).
- [3] For an extended bibliography see *Lattice Gas Methods for Partial Differential Equations*, edited by G. D. Doolen (Addison Wesley, Reading, MA, 1989).
- [4] R. Kingdon (private communication).
- [5] Y. H. Qian, D. d'Humieres, and P. Lallemand, *Europhys. Lett.* **17**, 479 (1992).
- [6] P. Espanol, *Phys. Rev. E* **52**, 1734 (1995).
- [7] A. K. Gunstensen, D. H. Rothman, S. Zaleski, and G. Zanetti, *Phys. Rev. A* **43**, 4320 (1991); D. H. Rothman and J. M. Keller, *J. Stat. Phys.* **52**, 111 (1988); A. K. Gunstensen and D. H. Rothman, *Europhys. Lett.* **18**, 157 (1992).
- [8] I. Halliday and C. M. Care, *Phys. Rev. E* **53**, 1602 (1996).
- [9] I. Halliday, C. M. Care, S. Thompson, and D. White, *Phys. Rev. E* **54**, 2573 (1996).
- [10] J. F. Olson and D. H. Rothman, *J. Stat. Phys.* **81**, 199 (1995).
- [11] D. Rothman and S. Zaleski, *Rev. Mod. Phys.* **81**, 181 (1995).
- [12] J. S. Rawlinson and B. Widom, *Molecular Theory of Capillarity* (Oxford University Press, New York, 1989).
- [13] J. Armstrong (unpublished).
- [14] C. Adler, D. d'Humieres, and D. H. Rothman, *J. Phys. I* **4**, 29 (1994).
- [15] A. K. Gunstensen, Ph.D. thesis, Massachusetts Institute of Technology 1992 (unpublished).
- [16] O. Behrend, R. Harris, and P. B. Warren, *Phys. Rev. E* **50**, 4586 (1994).